

Local density of states in the vortex lattice in a type II superconductor

Masanori Ichioka, Nobuhiko Hayashi, and Kazushige Machida
Department of Physics, Okayama University, Okayama 700, Japan
(October 15, 1996)

Local density of states (LDOS) in the triangular vortex lattice is investigated based on the quasi-classical Eilenberger theory. We consider the case of an isotropic s -wave superconductor with the material parameter appropriate to NbSe₂. At a weak magnetic field, the spatial variation of the LDOS shows cylindrical structure around a vortex core. On the other hand, at a high field where the core regions substantially overlap each other, the LDOS is sixfold star-shaped structure due to the vortex lattice effect. The orientation of the star coincides with the experimental data of the scanning tunneling microscopy. That is, the ray of the star extends toward the nearest-neighbor (next nearest-neighbor) vortex direction at higher (lower) energy.

PACS numbers: 74.60.Ec, 74.25.Jb, 61.16.Ch

I. INTRODUCTION

Since the success of observing the vortex core image by Hess *et al.* in the scanning tunneling microscopy (STM) experiments, it has been possible to investigate experimentally the local density of states (LDOS) around a vortex core in type II superconductors.¹⁻⁶ This investigation has revealed a rich internal electronic structure associated with a vortex core, and should be important for understanding the conventional and unconventional superconductors. Then, to extract further information from the experimental data, the detailed calculation of the LDOS is expected from the theoretical side.

Hess *et al.* have done a series of beautiful STM experiments on a layered hexagonal compound 2H-NbSe₂ ($T_c=7.3\text{K}$) to reveal the detailed spatially resolved electronic structure around a vortex core.¹⁻⁵ They provided direct images of individual vortices and the flux line lattice. Their experiment is the first one detecting the quasiparticle state bound to the vortex core, which was theoretically predicted by Caroli, de Gennes and Matricon.⁷ Further, the remarkable result is the sixfold star-shaped LDOS around a vortex.²⁻⁵ Their results are summarized as follows when the magnetic field is applied perpendicular to the hexagonal plane: (1) The LDOS for quasiparticle excitations has a sixfold star-shape centered at a core. (2) The orientation of this star depends on the bias energy. At zero bias, the “ray” of the star extends away from the nearest-neighbor direction where the conventional 60° Abrikosov vortex lattice is formed. Upon increasing the bias voltage, the star rotates by 30° and the ray extends to the nearest-neighbor direction. (See Fig. 4 in Ref. 2 or Fig. 1 in Ref. 4.) (3) In the intermediate bias voltage, a ray splits into a pair of nearly parallel rays, keeping its direction fixed (see the STM image for 0.48 mV in Fig. 1 of Ref. 4).

Recently, on the other hand, Maggio-Aprile *et al.* have succeeded in observing the STM image of the vortex cores on a high- T_c superconductor YBa₂Cu₃O₇.⁸ One of the point in analyzing their STM image of vortex is how the gap anisotropy ($d_{x^2-y^2}$ -wave in the high T_c superconductor) affects the LDOS around a vortex.

To understand these experimental results, the concrete form of the LDOS structure is expected to be calculated from the theoretical side. So far, the LDOS around a vortex was calculated by Gygi and Schlüter,^{9,10} and Shore *et al.*¹¹ from the Bogoliubov-de Gennes (BdG) equation. The calculations of the LDOS based on the quasi-classical Eilenberger (QCE) theory¹² were done by Klein,¹³ and Ullah *et al.*¹⁴ for an isotropic s -wave superconductors. While these calculations showed that the vortex image observed by STM is due to the quasiparticle state bound to the vortex core, they investigated only the case of an isolated single vortex, and based on the assumption of the cylindrically symmetric vortex core structure. In a $d_{x^2-y^2}$ -wave superconductor, the LDOS around an isolated single vortex was calculated by Schopohl and Maki,^{15,16} and Ichioka *et al.*¹⁷ However, the LDOS in the vortex lattice case has not been calculated so far.

On the other hand, the STM experiments associated with the vortex core are usually performed at high magnetic fields, where the distance between vortices is short and the overlap of the vortex core with that of the nearest-neighbor vortices can not be neglected. In this situation, the LDOS around a vortex core is expected to break cylindrical symmetry and show sixfold symmetric structure when the vortex lattice forms an triangular lattice. The purpose of this paper is to calculate the LDOS in the triangular vortex lattice by using the QCE theory, and clarify its sixfold symmetric structure. It is expected to be observed at a high magnetic field. For the case cylindrical symmetry is broken, the QCE approach is more suitable than the BdG approach.

As for the sixfold symmetric structure of the LDOS observed by Hess *et al.*,²⁻⁵ Gygi and Schlüter^{10,18} discussed it on the basis of the BdG theory by introducing a sixfold symmetric perturbation term and using their numerical solutions of the cylindrical symmetric case. While they explained the above-mentioned experimental features (1) and (2), the origin of their perturbation term is not clear, and it is uncertain whether the sixfold symmetric term can be treated by a perturbation theory. We note that their theory cannot determine the absolute orientation of the star relative to the vortex lattice configuration, since in their theory the orientation is determined by the sign of the perturbation term, which is given as an assumption.

As for the origin of the sixfold symmetric vortex structure, the following three possibilities are enumerated within the weak coupling BCS theory; the effect of the vortex lattice (that is, the effect of nearest-neighbor vortices), the effect of a sixfold symmetrically anisotropic *s*-wave pairing, and the effect of the sixfold symmetrically anisotropic density of states at the Fermi surface. In this paper, we focus on the effect of the vortex lattice by calculating the LDOS naively in the vortex lattice case. The contribution of this effect should be clarified before considering other anisotropic effects. The contribution of the other anisotropic effects is investigated elsewhere.¹⁹

The quasi-classical calculation in the vortex lattice case was so far performed by Klein in the case of low- κ type II superconductors such as Ta or Nb.²⁰ He calculated the spatial variation of the pair potential and magnetic field, where the Eilenberger equation is solved self-consistently in the Matsubara frequency and he succeeded in solving it by either the so-called symmetry method or the so-called explosion method.^{20,21} He also tried the calculation of the LDOS,^{22,23} where the Eilenberger equation is solved in real energy instead of the Matsubara frequency by using the self-consistently obtained pair potential and vector potential. In this real energy case, he could calculate only the momentum-resolved LDOS for specific \mathbf{k} (the relative momentum of the Cooper pair) direction because only the symmetry method was used. In this paper, we calculate the LDOS following the method suggested by Klein.^{20,22,23} However, as we succeed in solving the Eilenberger equation in the real energy case for arbitrary \mathbf{k} directions by using the explosion method, we can calculate the momentum-resolved LDOS for arbitrary \mathbf{k} directions. Then we can obtain the LDOS integrated over all \mathbf{k} directions.

The LDOS in the vortex lattice is an important physical quantity, since it can be observed directly by the STM experiments. And further, it can be a clue of estimating the transfer of the quasi-particle bound states between vortex cores. This transfer leads to the band structure of the bound states as suggested by Canel.²⁴ If the enough transfer exists, it makes the de Haas-van Alphen (dHvA) oscillation possible even in the superconducting state, which is observed in the materials such as NbSe₂²⁵ and YBa₂Cu₃O₇.²⁶

In our calculations, we consider the same situation as that Hess *et al.* performed their STM experiments on NbSe₂.¹⁻⁵ We use the material parameter appropriate to NbSe₂, and assume that the Fermi surface is two dimensional, which is appropriate to NbSe₂. The magnetic field is applied perpendicular to the hexagonal plane, that is, along the *z* axis. The case of the triangular vortex lattice in an isotropic *s*-wave superconductor is considered in the clean limit. The Fermi surface and the energy gap of the superconductivity are assumed to be isotropic in order to exclude other origins of anisotropy and to clarify the vortex lattice effect on the LDOS around a vortex. Throughout the paper, energies and lengths are measured in units of the uniform gap Δ_0 at $T = 0$ and the coherence length $\xi_0 = v_F/\Delta_0 = \pi\xi_{\text{BCS}}$ (v_F is the Fermi velocity and ξ_{BCS} BCS coherence length), respectively. The magnetic field and the vector potential are, respectively, scaled by ϕ_0/ξ^2 and ϕ_0/ξ , where ϕ_0 is the flux quantum.

The rest of this paper is organized as follows. In Sec. II, we describe the method of calculation based on the QCE theory. Section III contains numerically obtained results about the LDOS of the vortex lattice. The summary and discussions are given in Sec. IV.

II. QUASI-CLASSICAL EILENBERGER THEORY

The calculation based on the Eilenberger theory is performed by following the method suggested by Klein.^{20,22,23} First, we obtain the pair potential and vector potential self-consistently by solving the Eilenberger equation in the Matsubara frequency. Next, using them, we calculate the LDOS by solving the Eilenberger equation in the real energy instead of the Matsubara frequency.

In our calculation, the unit vectors of the vortex lattice are given by $\mathbf{r}_1 = (a_x, 0)$, $\mathbf{r}_2 = (\zeta a_x, a_y)$. As we consider a triangular lattice, we set $a_y/a_x = \sqrt{3}/2$ and $\zeta = 1/2$. The microscopic magnetic field $\mathbf{H}(\mathbf{r}) = (0, 0, H(\mathbf{r}))$ is divided into an external field $\bar{\mathbf{H}} = (0, 0, \bar{H})$ and an internal field $\mathbf{h}(\mathbf{r}) = (0, 0, h(\mathbf{r}))$,

$$\mathbf{H}(\mathbf{r}) = \nabla \times \mathbf{A}(\mathbf{r}) = \bar{\mathbf{H}} + \mathbf{h}(\mathbf{r}), \quad (2.1)$$

where the spatial average of $\mathbf{h}(\mathbf{r})$ vanishes. Therefore, the vector potential $\mathbf{A}(\mathbf{r})$ is also divided into two parts,

$$\mathbf{A}(\mathbf{r}) = \frac{1}{2}\bar{\mathbf{H}} \times \mathbf{r} + \mathbf{a}(\mathbf{r}) \quad (2.2)$$

in the symmetric gauge. From Eqs. (2.1) and (2.2), we obtain $\mathbf{h}(\mathbf{r}) = \nabla \times \mathbf{a}(\mathbf{r})$.

We consider the quasi-classical Green functions $g(\omega_n, \theta, \mathbf{r})$, $f(\omega_n, \theta, \mathbf{r})$ and $f^\dagger(\omega_n, \theta, \mathbf{r})$ with the Matsubara frequency $\omega_n = (2n+1)\pi T$, where \mathbf{r} is the center of mass coordinate of a Cooper pair. The direction of the relative momentum of the Cooper pair, $\hat{\mathbf{k}} = \mathbf{k}/|\mathbf{k}|$, is denoted by an angle θ measured from the x axis in the hexagonal plane. For the quasi-classical Green functions, the Eilenberger equation is given as

$$\left\{ \omega_n + \frac{1}{2} \left(\partial_{\parallel} + i \frac{2\pi}{\phi_0} A_{\parallel} \right) \right\} f(\omega_n, \theta, \mathbf{r}) = \Delta(\mathbf{r}) g(\omega_n, \theta, \mathbf{r}), \quad (2.3)$$

$$\left\{ \omega_n - \frac{1}{2} \left(\partial_{\parallel} - i \frac{2\pi}{\phi_0} A_{\parallel} \right) \right\} f^\dagger(\omega_n, \theta, \mathbf{r}) = \Delta^*(\mathbf{r}) g(\omega_n, \theta, \mathbf{r}), \quad (2.4)$$

$$\partial_{\parallel} g(\omega_n, \theta, \mathbf{r}) = \Delta^*(\mathbf{r}) f(\omega_n, \theta, \mathbf{r}) - \Delta(\mathbf{r}) f^\dagger(\omega_n, \theta, \mathbf{r}), \quad (2.5)$$

$$g(\omega_n, \theta, \mathbf{r}) = \left(1 - f(\omega_n, \theta, \mathbf{r}) f^\dagger(\omega_n, \theta, \mathbf{r}) \right)^{1/2}, \quad \text{Reg}(\omega_n, \theta, \mathbf{r}) > 0, \quad (2.6)$$

where $\partial_{\parallel} = d/dr_{\parallel}$ and $A_{\parallel} = \hat{\mathbf{k}} \cdot \mathbf{A} = -\frac{1}{2} H r_{\perp} + \hat{\mathbf{k}} \cdot \mathbf{a}$. Here, we have taken the coordinate system: $\hat{\mathbf{u}} = \cos \theta \hat{\mathbf{x}} + \sin \theta \hat{\mathbf{y}}$, $\hat{\mathbf{v}} = -\sin \theta \hat{\mathbf{x}} + \cos \theta \hat{\mathbf{y}}$, thus a point $\mathbf{r} = x \hat{\mathbf{x}} + y \hat{\mathbf{y}}$ is denoted as $\mathbf{r} = r_{\parallel} \hat{\mathbf{u}} + r_{\perp} \hat{\mathbf{v}}$. The first-order differential equations (2.3)-(2.5) are solved along the trajectory where r_{\perp} is held constant.

The self-consistent conditions for the pair potential $\Delta(\mathbf{r})$ and the vector potential are, respectively, given as

$$\Delta(\mathbf{r}) = V N_0 2\pi T \sum_{\omega_n > 0} \int_0^{2\pi} \frac{d\theta}{2\pi} f(\omega_n, \theta, \mathbf{r}), \quad (2.7)$$

$$\nabla \times \nabla \times \mathbf{A}(\mathbf{r}) = \nabla \times \nabla \times \mathbf{a}(\mathbf{r}) = -\frac{\pi}{\kappa^2} 2\pi T \sum_{\omega_n > 0} \int_0^{2\pi} \frac{d\theta}{2\pi} \frac{\hat{\mathbf{k}}}{i} g(\omega_n, \theta, \mathbf{r}), \quad (2.8)$$

where N_0 is the density of states at the Fermi surface, V the pairing interaction, and $\kappa = (7\zeta(3)/72)^{1/2} (\Delta_0/k_B T_c) \kappa_0 = 0.603\kappa_0$ with Riemann's zeta function $\zeta(3)$. The GL parameter κ_0 is given by

$$\kappa_0^{-2} = \frac{7\pi\zeta(3)}{9} N_0 \left(\frac{e}{\hbar c} \right)^2 \frac{(\hbar v_F)^4}{(\pi k_B T_c)^2}. \quad (2.9)$$

In our calculation, we use the relation

$$\frac{1}{V N_0} = \ln \frac{T}{T_c} + 2\pi T \sum_{0 < \omega_n < \omega_c} \frac{1}{|\omega_n|}, \quad (2.10)$$

and set the energy cutoff $\omega_c = 20T_c$. When $\mathbf{A}(\mathbf{r})$ is calculated from the differential equation (2.8), the Fourier transformation is employed by following the method of Klein.²⁰

We calculate the r.h.s. of Eqs. (2.7) and (2.8) using the quasi-classical Green functions obtained by Eqs. (2.3)-(2.6), and obtain the new value for $\Delta(\mathbf{r})$ and $\mathbf{A}(\mathbf{r})$. Using the renewed pair potential and vector potential, we solve the Eilenberger equation (2.3)-(2.6) again. Starting from the initial form,

$$\Delta(\mathbf{r}) = \left(\frac{2a_y}{a_x} \right)^{1/4} \sum_{p=-\infty}^{\infty} \exp \left\{ -\pi \frac{a_y}{a_x} \left(\frac{y+y_0}{a_y} + p \right)^2 - 2\pi i \left[p \left(\frac{x_0}{a_x} + \frac{\zeta}{2} p \right) + \left(\frac{y_0}{a_y} + p \right) \right] \right\} \exp \left(-i\pi \frac{xy}{a_x a_y} \right) \quad (2.11)$$

and $\mathbf{a}(\mathbf{r}) = 0$, we repeat this simple iteration procedure more than 20 times, and obtain a sufficiently self-consistent solution for $\Delta(\mathbf{r})$ and $\mathbf{A}(\mathbf{r})$. In Eq. (2.11), the r.h.s. is the Abrikosov solution of the vortex lattice, where we use the relation $H a_x a_y / \phi_0 = 1$. The factor $\exp(-i\pi xy / a_x a_y)$ is due to the gauge transformation from the Landau gauge to the symmetric gauge. We set $\mathbf{r}_0 = (x_0, y_0) = -\frac{1}{2}(\mathbf{r}_1 + \mathbf{r}_2)$ so that one of the vortex centers locates at the origin of the coordinate.

On the other hand, the LDOS for energy E is given by

$$N(E, \mathbf{r}) = \int_0^{2\pi} \frac{d\theta}{2\pi} N(E, \mathbf{r}, \theta) = \int_0^{2\pi} \frac{d\theta}{2\pi} \text{Re } g(i\omega_n \rightarrow E + i\eta, \theta, \mathbf{r}), \quad (2.12)$$

where η is a positive infinitesimal constant, $N(E, \mathbf{r}, \theta)$ the angular-resolved LDOS. Typically, we choose $\eta = 0.01$. To obtain $g(i\omega_n \rightarrow E + i\eta, \theta, \mathbf{r})$, we solve Eqs.(2.3)-(2.6) for $\eta - iE$ instead of ω_n using the self-consistently obtained pair potential and vector potential.

In our calculations, we discretize $\mathbf{r} = u\mathbf{r}_1 + v\mathbf{r}_2$ in a unit cell ($-0.5 \leq u \leq 0.5$, $-0.5 \leq v \leq 0.5$) for $\Delta(\mathbf{r})$ and $\mathbf{a}(\mathbf{r})$. There, u and v are discretized into the 41 mesh points, respectively. When we solve Eqs.(2.3)-(2.6), we need to know $\Delta(\mathbf{r})$ and $\mathbf{a}(\mathbf{r})$ for arbitrary \mathbf{r} . It is given by interpolation of the value on the mesh point. It is enough that $\Delta(\mathbf{r})$ and $\mathbf{a}(\mathbf{r})$ are calculated within a unit cell. Once we obtain $\Delta(\mathbf{r})$ and $\mathbf{a}(\mathbf{r})$ in a unit cell, we can know $\Delta(\mathbf{r})$ and $\mathbf{a}(\mathbf{r})$ in other unit cells by the following relation of the lattice translation $\mathbf{R} = m\mathbf{r}_1 + n\mathbf{r}_2$ (m, n : integer), respectively,

$$\Delta(\mathbf{r} + \mathbf{R}) = \Delta(\mathbf{r})e^{i\chi(\mathbf{r}, \mathbf{R})}, \quad \mathbf{a}(\mathbf{r} + \mathbf{R}) = \mathbf{a}(\mathbf{r}), \quad (2.13)$$

where

$$\chi(\mathbf{r}, \mathbf{R}) = -\frac{2\pi}{\phi_0} \mathbf{A}(\mathbf{R}) \cdot \mathbf{r} - \pi mn + \frac{2\pi}{\phi_0} (\mathbf{H} \times \mathbf{r}_0) \cdot \mathbf{R} \quad (2.14)$$

in the symmetric gauge.

Since we need a lot of CPU time for the integrating process of Eqs. (2.3)-(2.5) in the calculation of the quasi-classical Green functions, we want to shorten this process as much as possible. It becomes possible by the symmetry consideration, as suggested by Klein.²⁰ Without the integrating process of all θ and \mathbf{r} cases, we can obtain the Green functions for all θ and \mathbf{r} .

When one of the vortex center locates at the origin of the coordinate ($\mathbf{r}_0 = -\frac{1}{2}(\mathbf{r}_1 + \mathbf{r}_2)$), the pair potential has the relation

$$\Delta(\mathbf{r}) = -\Delta(-\mathbf{r}). \quad (2.15)$$

Considering the transformation $\mathbf{r} \rightarrow -\mathbf{r}$, we obtain the following relation from Eqs. (2.3)-(2.6) and (2.15),

$$\begin{aligned} f(\omega_n, \theta, \mathbf{r}) &= -f^{\dagger*}(\omega_n^*, \theta, -\mathbf{r}), \\ f^{\dagger}(\omega_n, \theta, \mathbf{r}) &= -f^*(\omega_n^*, \theta, -\mathbf{r}), \\ g(\omega_n, \theta, \mathbf{r}) &= g^*(\omega_n^*, \theta, -\mathbf{r}). \end{aligned} \quad (2.16)$$

In the calculation of the Matsubara frequency ω_n or the case $E = 0$, once we calculate the Green functions for \mathbf{r} in a half area of a unit cell from Eqs. (2.3)-(2.6), we can know the Green functions for all \mathbf{r} in the unit cell from the relation (2.16).

When we consider the reflection at the x axis $S\mathbf{r} = (x, -y)$, our definition of $\Delta(\mathbf{r})$ gives the relation

$$\Delta(\mathbf{r}) = -\Delta^*(S\mathbf{r}). \quad (2.17)$$

Then we obtain the relation

$$\begin{aligned} f(\omega_n, \theta, \mathbf{r}) &= -f^*(\omega_n, -\theta, S\mathbf{r}), \\ f^{\dagger}(\omega_n, \theta, \mathbf{r}) &= -f^{\dagger*}(\omega_n, -\theta, S\mathbf{r}), \\ g(\omega_n, \theta, \mathbf{r}) &= g^*(\omega_n, -\theta, S\mathbf{r}) \end{aligned} \quad (2.18)$$

from Eqs. (2.3)-(2.6). On the other hand, there is a relation

$$\Delta(\mathbf{r}) = \Delta(R^n \mathbf{r})e^{in\pi/3}, \quad (2.19)$$

when we consider the rotation $n\pi/3$ (n : integer) around the origin of the coordinate; $R^n \mathbf{r} = (x \cos(n\pi/3) - y \sin(n\pi/3), x \sin(n\pi/3) + y \cos(n\pi/3))$. Then we obtain the relation

$$\begin{aligned} f(\omega_n, \theta, \mathbf{r}) &= f(\omega_n, \theta + n\pi/3, R^n \mathbf{r})e^{in\pi/3}, \\ f^{\dagger}(\omega_n, \theta, \mathbf{r}) &= f^{\dagger}(\omega_n, \theta + n\pi/3, R^n \mathbf{r})e^{-in\pi/3}, \\ g(\omega_n, \theta, \mathbf{r}) &= g(\omega_n, \theta + n\pi/3, R^n \mathbf{r}) \end{aligned} \quad (2.20)$$

from Eqs. (2.3)-(2.6). Once we calculate the Green functions for $0 \leq \theta \leq \pi/6$ from Eqs. (2.3)-(2.6), we can know the Green functions for all θ from the relations (2.18) and (2.20).

There are two methods to solve the Eilenberger equation (2.3)-(2.6); the explosion method and the symmetry method. We describe them in the following.

A. explosion method

We use the so-called explosion method^{20,21} in this paper to obtain the quasi-classical Green function

$$\hat{g} \equiv \begin{pmatrix} g & if \\ -if^\dagger & -g \end{pmatrix} \quad (2.21)$$

from the Eilenberger equation (2.3)-(2.6). In addition to a physical solution \hat{g}_{ph} , Eqs. (2.3)-(2.6) have two unphysical solutions \hat{g}_+ and \hat{g}_- . The solutions \hat{g}_\pm explode (increase exponentially) in the directions $\pm\mathbf{k}$ and decrease in the opposite directions. Even when we use the physical solution as an initial value, the unphysical solutions always mix and become dominant during the process of the numerical integration of Eqs. (2.3)-(2.5) along a long path. We obtain \hat{g}_\pm by integrating from $r_{\parallel} \mp r_A$ to r_{\parallel} , where $r_A (> 0)$ is large so that explosion takes place. It is known^{20,21} that the physical solution is obtained from the commutator of the two unphysical solutions,

$$\hat{g}_{\text{ph}} = c[\hat{g}_+, \hat{g}_-], \quad (2.22)$$

where c is a constant determined from Eq. (2.6). In this method, we can obtain the solution for arbitrary \mathbf{k} directions.

B. symmetry method

In the case of solving the Eilenberger equation in the real energy E , Klein could not succeed in the explosion method. Then, he calculated the angular-resolved LDOS by means of the so-called symmetry method.^{22,23} The lattice translation $\mathbf{R} = m\mathbf{r}_1 + n\mathbf{r}_2$ (m, n : integer) of the quasi-classical Green function is given as

$$\begin{aligned} f(\omega_n, \theta, \mathbf{r} + \mathbf{R}) &= f(\omega_n, \theta, \mathbf{r})e^{i\chi(\mathbf{r}, \mathbf{R})}, \\ f^\dagger(\omega_n, \theta, \mathbf{r} + \mathbf{R}) &= f^\dagger(\omega_n, \theta, \mathbf{r})e^{-i\chi(\mathbf{r}, \mathbf{R})}, \\ g(\omega_n, \theta, \mathbf{r} + \mathbf{R}) &= g(\omega_n, \theta, \mathbf{r}), \end{aligned} \quad (2.23)$$

where $\chi(\mathbf{r}, \mathbf{R})$ is defined in Eq. (2.14). When we solve Eqs. (2.3)-(2.6) for the \mathbf{k} direction parallel to $m\mathbf{r}_1 + n\mathbf{r}_2$, the solution have to satisfy Eq. (2.23) as the boundary condition. Thus, we integrate the first differential equations (2.3)-(2.5) along the trajectory from \mathbf{r} to $\mathbf{r} + \mathbf{R}$, and search the solution which satisfies the boundary condition (2.23) by the so-called shooting method or other method.

Compared with the explosion method, the integral path can be short in the symmetry method, especially for the calculation of the real energy E . Then the CPU time of the numerical calculation may be short. However, in the symmetry method, we can obtain the solution only for the specific \mathbf{k} direction parallel to $m\mathbf{r}_1 + n\mathbf{r}_2$. Since we must know the solution for all \mathbf{k} directions to calculate the LDOS in Eq. (2.12), we cannot obtain the LDOS in this method.

III. PAIR POTENTIAL, MAGNETIC FIELD AND LDOS

The pair potential, the vector potential and the LDOS are calculated for the material parameter appropriate to NbSe₂, i.e., the BCS coherence length 77 Å and the BCS penetration depth 690 Å.³ As an example of a low magnetic field, we consider the case $\bar{H} = 0.1$ Tesla ($a_x = 6.4\xi$). And as an example of a high magnetic field, we consider the case $\bar{H} = 1$ Tesla ($a_x = 2.0\xi$). As for the example of further high field, the cases $\bar{H} = 2$ Tesla ($a_x = 1.4\xi$) and 4 Tesla ($a_x = 1.0\xi$) are also considered. Figure 1 presents the configuration of the vortex lattice presented in figures in this paper. In the figures, there are 7 vortex centers, and one of the vortex centers locates at the center of each figure. When we consider the profile of the spatial variation, we present it along the trajectories of line OA (0° radial direction), line OB (15° radial direction), line OC (30° radial direction) and line AC (boundary).

A. Pair potential and magnetic field

The amplitude of the self-consistently obtained pair potential $|\Delta(\mathbf{r})|$ is shown in the contour plot of Fig. 2. For $\bar{H} = 0.1$ Tesla in Fig. 2 (a), the core region localizes in the small region around the vortex center in the unit cell. For $\bar{H} = 1$ Tesla in Fig. 2 (b), the core region occupies the large part of the unit cell. Then the core regions substantially overlap each other. As seen from the contour lines, while the inner region of the vortex core (the region where

$|\Delta(\mathbf{r})| < 0.8$) has cylindrically symmetric structure, the outer region ($|\Delta(\mathbf{r})| \geq 0.8$) shows the sixfold symmetric structure. There, the amplitude along the nearest-neighbor vortex direction (0° direction) is a little suppressed compared with that along the next nearest-neighbor vortex direction (30° direction). In this high field case, the maximum of the amplitude is suppressed down to $0.95\Delta_0$. The sixfold symmetric structure of $|\Delta(\mathbf{r})|$ appears more clearly in the case $\bar{H}=2$ Tesla in Fig. 2 (c), where the maximum of the amplitude is suppressed down to $0.83\Delta_0$. In the case $\bar{H}=4$ Tesla, the pair potential has similar sixfold symmetric spatial distribution, but its amplitude is suppressed down to $0.38\Delta_0$.

The spatial variation of the magnetic field is obtained from the self-consistently obtained vector potential. The microscopic magnetic field $H(\mathbf{r})$ is shown in Fig. 3. For $\bar{H}=0.1$ Tesla in Fig. 3 (a), $H(\mathbf{r})$ has a cylindrically symmetric sharp peak at each vortex center. The variation of $H(\mathbf{r})$ is in the range $0.75 \leq H(\mathbf{r})/\bar{H} \leq 2.95$. For $\bar{H}=1$ Tesla in Fig. 3 (b), this peak becomes lower and broader ($0.981 \leq H(\mathbf{r})/\bar{H} \leq 1.096$). It has almost cylindrically symmetric but slightly sixfold symmetric structure. There $H(\mathbf{r})$ extends slightly to the 30° direction in the core region. The sixfold symmetric distribution of $H(\mathbf{r})$ is seen clearly in the case $\bar{H}=2$ Tesla in Fig. 3 (c), where the peak of $H(\mathbf{r})$ becomes further low and broad structure ($0.994 \leq H(\mathbf{r})/\bar{H} \leq 1.025$).

B. Sixfold symmetric LDOS

The LDOS in Eq. (2.12) is calculated by using the self-consistently obtained pair potential and vector potential presented in Figs. 2 and 3.

As for the angular-resolved LDOS $N(E, \mathbf{r}, \theta)$ in Eq. (2.12), the results of Klein in the symmetry method²² are qualitatively reproduced by our calculation of the explosion method. In the single vortex case, $N(E, \mathbf{r}, \theta)$ consists of a straight sharp ridge line parallel to the \mathbf{k} -direction, where its distance from the vortex center increases on raising E . At a high magnetic field of the vortex lattice case, the ridge of $N(E, \mathbf{r}, \theta)$ extends to the neighboring unit cells (see, for example, Fig. 5 in Ref. 22). Especially it is noted that, when \mathbf{k} points toward the nearest-neighbor vortex direction ($\theta = 0^\circ$ or $\hat{\mathbf{k}}_{10}$ in the notation of Klein²²), the sharp ridge in the single vortex case splits into two parallel ridges. There, $N(E, \mathbf{r}, \theta)$ distributes broadly in the region between them (see Fig. 10 in Ref. 22). Also when \mathbf{k} points toward the next nearest-neighbor vortex direction ($\theta = 30^\circ$ or $\hat{\mathbf{k}}_{11}$), $N(E, \mathbf{r}, \theta)$ slightly splits into two ridges. The above-mentioned splitting of the ridge occurs more clearly for higher magnetic field or larger E . At a weak magnetic field, the ridge of $N(E, \mathbf{r}, \theta)$ localizes within a unit cell, and the splitting of the ridge does not occur even for $\theta = 0$ (see Fig. 1 in Ref. 22).

Integrating $N(E, \mathbf{r}, \theta)$ over all θ , we obtain the LDOS $N(E, \mathbf{r})$ in Eq. (2.12). The spatial variation of the numerically obtained LDOS is shown in Figs. 4 and 5 for the weak magnetic field case $\bar{H} = 0.1$ Tesla. Figure 4 shows the contour plot of $N(E, \mathbf{r})$ for each E . Figure 5 shows the profiles of $N(E, \mathbf{r})$ along the lines OA, OB, OC and AC of Fig. 1. As shown in Fig. 4 (a), the LDOS shows cylindrical structure in the low energy case ($E \leq 0.8$), where the ridge of the LDOS forms a ring around each vortex center. It is the similar structure as that obtained in the single vortex case for s -wave pairing (see, for example, Fig. 1 in Ref. 15). However, in the higher energy case shown in Figs. 4 (b) and (c), the radius of the ring approaches the boundary of a unit cell in the vortex lattice, and the LDOS becomes sixfold symmetric structure.

The LDOS for the high field case $\bar{H} = 1$ Tesla is shown in Figs. 6 and 7. It presents the sixfold symmetric star-shaped structure even in the low energy case. At $E = 0$, the ray of the star extends to the next nearest-neighbor directions (the 30° directions) as presented in Fig. 6 (a). The width of the ray is rather broad compared with the experimental data.²⁻⁵ At higher energy $E \sim 0.6$, on the other hand, the ray extends to the nearest-neighbor directions (the 0° directions) as shown in Fig. 6 (c). The orientation of the star relative to the vortex lattice is consistent with the experimental data by Hess *et al.*²⁻⁵ Therefore, the experimental features (1) and (2) mentioned in Sec. I, including the orientation of the star, are qualitatively reproduced without further assumptions. As presented in Fig. 6 (b), at the intermediate energy of the 30° rotation of the star, the amplitude of the ray in the 30° directions decreases and the new ray starts to extend in the 0° directions with increasing E . This behavior is in discord with the experimental data. In the experiment on NbSe₂, the LDOS shows the split parallel ray structure at the intermediate energy (the feature (3) mentioned in Sec. I).

The experimental data around $E \sim 1$ can be qualitatively reproduced by our calculation. For $E \sim 1$, there are little LDOS distribution around the vortex core region, and the LDOS distributes around the boundary of the Wigner-Seitz cell of the vortex lattice. Therefore, the vortex core is detected as a dark object in the STM image. Even in the case the vortex core localizes in the narrow region around the vortex center, the dark STM image of the vortex core for $E \sim 1$ has the size comparable to the unit cell, as shown in Figs. 4 (b) and (c). In the LDOS distribution around $E \sim 1$, we pay our attention to the value at the boundary of the Wigner-Seitz cell, that is, on the line AC in Fig. 1. For $E \leq 1$, $N(E, \mathbf{r})$ is large at the point A compared with the point C, as seen from Fig. 6 (d). On the other

hand, the peak of $N(E, \mathbf{r})$ shifts to the point C on raising E as seen from Fig. 6 (e), which is consistent with the experimental STM image for 1.2 mV in Fig. 1 of Ref. 4.

The spatial variation of the LDOS structure in Fig. 6 can be explained as follows. Without the vortex lattice effect, the LDOS forms the cylindrical structure which is shown schematically as white rings in Fig. 8. It has the ridge on a ring around each vortex center, and the LDOS distributes at the outer side of the rings. To this distribution, the vortex lattice effect suppresses the LDOS along the common tangent lines on these rings (lines in Fig. 8). These lines runs toward the 0° and its equivalent directions (the nearest-neighbor vortex directions). This suppression is due to the splitting of the ridges in the angle-resolved LDOS $N(E, \mathbf{r}, \theta)$ for θ of the nearest-neighbor directions. In the contribution to the LDOS, the ridge of $N(E, \mathbf{r}, \theta)$ along the lines of Fig. 8 becomes broad and low-height distribution due to the splitting (see Fig. 10 in Ref. 22). Therefore, it is seen that the LDOS in Fig. 6 has small value at the points along the lines. The small suppression is also shown along the tangent lines running toward the 30° and its equivalent directions (the next nearest-neighbor vortex directions). Considering the fact that the radius of the ring in Fig. 8 increases on elevating E , we can understand the change of the LDOS in Figs. 6 (a) to (e). Since the radius reduces to 0 in the limit $E \rightarrow 0$, the suppression lines in Fig. 8 reduce to the lines connecting nearest-neighbor vortex centers for $E = 0$, which is seen in Fig. 6 (a).

Another way to examine the quasiparticle excitations in the vortex state is to see how the spectrum evolves along the radial directions. We consider the spectrum at the points along the 0° (line OA in Fig. 1), 15° (line OB) and 30° (line OC) radial directions. In the figures, we show the spectrum at $\mathbf{r} = (ca_x, 0)$ for the 0° direction, $\mathbf{r} = (ca_x, ca_x \tan(\pi/12))$ for the 15° direction and $\mathbf{r} = (ca_x, ca_x \tan(\pi/6))$ for the 30° direction, where we choose the point for $c=0, 0.1, 0.3, 0.6, 1$. As for the case $\bar{H} = 0.1$ Tesla, Fig. 9 shows the spectrum at the points along the 0° direction. For $E \leq 0.8$, the spectrum has the similar structure as that of the single vortex case (see Fig. 2 in Ref. 14 for comparison). At higher energy, the peak at $E = 1$ in the single vortex case becomes broad and shifts a little to higher energy side due to the vortex lattice effect. Along the other radial directions, the LDOS has the almost similar spectrum as that of the 0° direction. Small differences are shown only for $E \geq 0.8$.

On the other hand, the spectrum for $\bar{H} = 1$ Tesla is shown in Fig. 10, where (a), (b) and (c) are that along 0° , 15° and 30° radial directions, respectively. It is notable that the lower energy peak in Fig. 9 splits into two or three peaks in this higher field case. The behavior of these peaks varies depending on the direction of the radial lines, as shown in Fig. 10 (a)-(c). The peak above $E = 1$ in Fig. 9 is suppressed in Fig. 10. The peak of the spectrum at the boundary point ($c = 1$) shifts to higher energy from 1.

C. LDOS at higher field

Here, to discuss the transfer of the quasiparticle bound states between vortex cores, we focus on the LDOS structure at $E = 0$. With increasing a magnetic field, the peak of the LDOS at the vortex center decreases ($N(E = 0, \mathbf{r} = 0) = 71$ for 0.1 Tesla, 65 for 1 Tesla, 44 for 2 Tesla and 11 for 4 Tesla), and the distribution of the LDOS extends sixfold symmetrically to the wider region. Therefore, the LDOS around the vortex core is connected each other at high magnetic field even in the zero energy state. To show the connection clearly, the LDOS for $\bar{H} = 2$ Tesla and 4 Tesla is presented in Figs. 11 and 12. At $\bar{H} = 2$ Tesla in Fig. 11 (a), the LDOS around the vortex core is connected each other at the middle point of the line AC of Fig. 1. At further high field $\bar{H} = 4$ Tesla shown in Fig. 11 (b), the LDOS is seems to have the component uniformly distributing all over the unit cell. There, the LDOS has small peak at the vortex center and minimum at the stationary point of the current flow (point A of Fig. 1). With raising a magnetic field, the LDOS at the boundary of the Wigner-Seitz cell increases (its maximum value is 0.01 for 0.1 Tesla, 0.18 for 1 Tesla, 0.44 for 2 Tesla and 0.90 for 4 Tesla), which means that the transfer of the quasiparticle bound states between vortex cores increases.

On NbSe₂, the dHvA oscillation is observed at magnetic fields down to 4 Tesla in the superconducting mixed state. As discussed above, we show that there is large transfer of the bound state between vortex cores in this high field region. This transfer seems to be a possible origin of the dHvA oscillation in superconductors.

IV. SUMMARY AND DISCUSSIONS

By using the self-consistently obtained pair potential and vector potential, the LDOS of the triangular vortex lattice is calculated in an isotropic s -wave superconductors based on the quasi-classical Eilenberger theory. Important results obtained for the vortex lattice are as follows; (i) We do find a sixfold star shape of the LDOS and the 30° rotation upon elevating the bias energy. The sixfold star originates from the triangular vortex lattice effect. (ii) The orientation of the star coincides with the STM data, namely the ray extends toward the next nearest-neighbor vortex direction

at lower bias energy. Therefore we succeed in determining the absolute direction relative to the vortex lattice. This is one of the most eminent features in the STM data by Hess *et al.*¹⁻⁵ Thus the experimental features (1) and (2) mentioned in Sec. I are qualitatively reproduced by the naive calculation of the LDOS in the triangular vortex lattice. (iii) For $E \sim 1$, the LDOS distributes around the boundary of the Wigner-Seitz cell of the vortex lattice, and there are little distribution around the vortex core region. Therefore, the vortex core is detected as a sixfold symmetric dark object in the STM images. At the energy $E \sim 1.2$, the LDOS has large intensity at the point farthest from the vortex center (the point C in Fig. 1). (iv) The characteristic sixfold symmetric LDOS structure in the low energy case appears only at a high magnetic field such as 1 Tesla for the material parameters appropriate to NbSe₂, where the core regions substantially overlap each other. At a lower magnetic field such as 0.1 Tesla, the LDOS reduces to the almost cylindrical structure in the low energy case.

As mentioned above, the numerically obtained LDOS in the vortex lattice case can qualitatively reproduce the characteristic features (1) and (2) in the experimental data on NbSe₂. However, the detailed comparison reveals some discrepancies between the experimental data and our results, as follows; (v) At the intermediate energy of the 30° rotation, our results does not reproduce the split parallel ray structure (the feature (3) mentioned in Sec. I). In the experiment, the ray of the star in the 30° direction at $E = 0$ splits into two parallel rays with elevating E . In our results, the ray along the 30° direction at $E = 0$ weakens and new ray starts to extend along the 0° direction with increasing E . (vi) The shape of the star in our results is rather different from the experimental data at $E = 0$. In the experimental data, the ray of the star sharply extends with the narrow width along the 30° direction. On the other hand, the ray extends with wide width in our results. (vii) In our results, the structure of the LDOS has cylindrical symmetry at a low magnetic field in the low energy case. However, in the experiment by Hess *et al.*, the clear star-shaped structure is observed at low fields down to 500 Gauss.

These discrepancies mean that we have to consider the other effects in addition to the vortex lattice effect studied here in order to reproduce the detailed LDOS structure of NbSe₂ observed by Hess *et al.* If we consider the effect of the anisotropic s -wave pairing which has sixfold symmetrically anisotropic gap in the basal plane, the STM images by Hess *et al.* are quite well reproduced. We report it in detail elsewhere.¹⁹ It suggests that the well-studied material NbSe₂ seems to be one particular system which has anisotropic pairing. Our calculation is performed for the idealized isotropic s -wave superconductor. The characteristic features numerically obtained in this paper are expected to be well observed in other materials which are isotropic s -wave superconductors.

To discuss the transfer of the quasiparticle bound states between vortex cores, we consider the LDOS structure at $E = 0$. At high magnetic fields, the LDOS around the vortex core is connected each other even in the zero energy state. With raising a magnetic field, this connection increases. It means that the transfer of the quasiparticle bound state between vortex cores increases. On NbSe₂, the dHvA oscillation is observed at magnetic fields down to 4 Tesla in the superconducting mixed state. We show that there is large transfer of the bound state between vortex cores in this high field region. This transfer seems to be a possible origin of the dHvA oscillation in superconductors. The estimate whether this transfer is enough for the dHvA oscillation or not is a future problem.

ACKNOWLEDGMENTS

We would like to thank H. F. Hess for fruitful discussions and information of their experiments. The authors are indebted to the Supercomputer Center of the Institute for Solid State Physics, University of Tokyo, and Kyoto University Data Processing Center, for a part of the numerical calculations. One of the authors (M. I.) is supported by a Research Fellowship of the Japan Society for the Promotion of Science for Young Scientists.

FIG. 1. The configuration of the vortex lattice in our figures. The vortex centers are shown by \bullet . A hexagon enclosed by dashed lines presents the Wigner-Seitz cell of the vortex lattice. When we consider the profile of the spatial variation, we present it along the trajectories of line OA (0° radial direction), line OB (15° radial direction), line OC (30° radial direction) and line AC (boundary).

FIG. 2. Spatial variation of the pair potential at $T/T_c = 0.1$. Contour plot of the amplitude, $|\Delta(\mathbf{r})|$, is presented. (a) $\bar{H} = 0.1$ Tesla. The region $12.8\xi \times 12.8\xi$ is presented. The core region localizes in a small area around each vortex center. (b) $\bar{H} = 1$ Tesla. The region $4\xi \times 4\xi$ is presented. (c) $\bar{H} = 2$ Tesla. The region $2.8\xi \times 2.8\xi$ is presented. For $\bar{H} = 1$ Tesla and 2 Tesla, the core region occupies the large part of the unit cell. The pair potential shows cylindrical symmetry at the inner region of the vortex core, and sixfold symmetry at the outer region.

FIG. 3. Spatial variation of the magnetic field at $T/T_c = 0.1$. Contour plot of the normalized value $H(\mathbf{r})/\bar{H}$ is presented for $\bar{H} = 0.1$ Tesla (a), 1 Tesla (b) and 2 Tesla (c). For $\bar{H} = 1$ Tesla and 2 Tesla, $H(\mathbf{r})$ extends a little to the 30° direction in the vortex core region.

FIG. 4. Spatial variation of the LDOS $N(E, \mathbf{r})$ at $\bar{H} = 0.1$ Tesla. The contour plot is shown for $E=0.8$ (a), 1.0 (b) and 1.2 (c). The LDOS structure shows cylindrical symmetry for lower energy $E \leq 0.8$, and sixfold symmetry for higher energy $E \geq 1$.

FIG. 5. Spatial variation of the LDOS $N(E, \mathbf{r})$ at $\bar{H} = 0.1$ Tesla. The profiles along the lines OA (solid line), OB (dotted line), OC (dot-dashed line) and AC (thick line) of Fig. 1 are presented for $E=0.8$ (a), 1.0 (b) and 1.2 (c) as a function of r (distance from the vortex center). Each figure corresponds to that of Fig. 4.

FIG. 6. Spatial variation of the LDOS $N(E, \mathbf{r})$ at $\bar{H} = 1$ Tesla. The contour plot is shown for $E=0$ (a), 0.2 (b), 0.6 (c), 1.0 (d) and 1.2 (e). In this high magnetic field case, the LDOS shows sixfold symmetry even at the low energy down to $E = 0$.

FIG. 7. Spatial variation of the LDOS $N(E, \mathbf{r})$ at $\bar{H} = 1$ Tesla. The profiles along the lines OA (solid line), OB (dotted line), OC (dot-dashed line) and AC (thick line) of Fig. 1 are presented for $E=0$ (a), 0.2 (b), 0.6 (c), 1.0 (d) and 1.2 (e) as a function of r . Each figure corresponds to that of Fig. 6.

FIG. 8. Schematically presented LDOS structure, which corresponds to that of Fig. 6. Without the vortex lattice effect, the LDOS has the cylindrical structure, which is presented as white rings. To this structure, the vortex lattice effect suppresses the LDOS along the lines presented in the figure. Therefore, it is seen that the LDOS in Fig. 6 has small value at the points along the lines.

FIG. 9. Spectrum $N(E, \mathbf{r})$ at the points \mathbf{r} along the 0° radial direction line OA for $\bar{H} = 0.1$ Tesla. The sample points are given by $\mathbf{r} = (ca_x, 0)$ with $c=0, 0.1, 0.3, 0.6$ and 1.

FIG. 10. Spectrum $N(E, \mathbf{r})$ at the points \mathbf{r} along the 0° radial direction line OA (a), the 15° line OB (b) and the 30° line OC (c) for $\bar{H} = 1$ Tesla. The sample points are given by $\mathbf{r} = (ca_x, 0)$ for (a), $(ca_x, ca_x \tan(\pi/12))$ for (b) and $(ca_x, ca_x \tan(\pi/6))$ for (c), with $c=0, 0.1, 0.3, 0.6$ and 1.

FIG. 11. Spatial variation of the LDOS $N(E, \mathbf{r})$ for $E = 0$. Contour plot is shown for $\bar{H} = 2$ Tesla (a) and 4 Tesla (b). At higher magnetic fields, the LDOS around the vortex is connected each other.

FIG. 12. Spatial variation of the LDOS $N(E, \mathbf{r})$ for $E = 0$. Profile along the line OA (solid line), OB (dotted line), OC (dot-dashed line) and AC (thick line) of Fig. 1. are presented for $\bar{H} = 2$ Tesla (a) and 4 Tesla (b) as a function of r . Each figure corresponds to that of Fig. 11.

-
- ¹ H. F. Hess, R. B. Robinson, R. C. Dynes, J. M. Valles, Jr., and J. V. Waszczak, Phys. Rev. Lett. **62**, 214 (1989).
- ² H. F. Hess, R. B. Robinson, and J. V. Waszczak, Phys. Rev. Lett. **64**, 2711 (1990).
- ³ H. F. Hess, R. B. Robinson, and J. V. Waszczak, Physica B **169**, 422 (1991).
- ⁴ H. F. Hess, Physica C **185-189**, 259 (1991).
- ⁵ H. F. Hess, in *Scanning Tunneling Microscopy*, ed. J. A. Stroscio and W. J. Kaiser (Academic Press, San Diego, 1993) p. 427.
- ⁶ Ch. Renner, A. D. Kent, Ph. Niedermann, Ø. Fischer, and F. Lévy, Phys. Rev. Lett. **67**, 1650 (1991).
- ⁷ C. Caroli, P. G. de Gennes, and J. Matricon, Phys. Lett. **9**, 307 (1964).
- ⁸ I. Maggio-Aprile, Ch. Renner, A. Erb, E. Walker, and Ø. Fischer, Phys. Rev. Lett. **75**, 2754 (1995).
- ⁹ F. Gygi and M. Schlüter, Phys. Rev. B **41**, 822 (1990).
- ¹⁰ F. Gygi and M. Schlüter, Phys. Rev. B **43**, 7609 (1991).
- ¹¹ J. D. Shore, M. Huang, A. T. Dorsey, and J. P. Sethna, Phys. Rev. Lett. **62**, 3089 (1989).
- ¹² G. Eilenberger, Z. Phys. **214**, 195 (1968).
- ¹³ U. Klein, Phys. Rev. B **41**, 4819 (1990).
- ¹⁴ S. Ullah, A. T. Dorsey, and L. J. Buchholtz, Phys. Rev. B **42**, 9950 (1990).
- ¹⁵ N. Schopohl and K. Maki, Phys. Rev. B **52**, 490 (1995).
- ¹⁶ K. Maki, N. Schopohl, and H. Won, Physica B **204**, 214 (1995).
- ¹⁷ M. Ichioka, N. Hayashi, N. Enomoto, and K. Machida, Phys. Rev. B **53**, 15316 (1996).
- ¹⁸ F. Gygi and M. Schlüter, Phys. Rev. Lett. **65**, 1820 (1990).
- ¹⁹ N. Hayashi, M. Ichioka, and K. Machida, Phys. Rev. Lett. **77**, 4074 (1996).
- ²⁰ U. Klein, J. Low Temp. Phys. **69**, 1 (1987).
- ²¹ E. V. Thuneberg, J. Kurkijärvi, and D. Rainer, Phys. Rev. B **29**, 3913 (1984).
- ²² U. Klein, Phys. Rev. B **40**, 6601 (1989).
- ²³ B. Pöttinger and U. Klein, Phys. Rev. Lett. **70**, 2806 (1993).
- ²⁴ E. Canel, Phys. Lett. **16**, 101 (1965).
- ²⁵ J. E. Graebner and M. Robbins, Phys. Rev. Lett. **36**, 422 (1976).
- Y. Ōnuki, I. Umehara, T. Ebihara, N. Nagai, and K. Takita, J. Phys. Soc. Jpn. **61**, 692 (1992).
- ²⁶ C. M. Fowler, B. L. Freeman, W. L. Hults, J. C. King, F. M. Mueller, and J. L. Smith, Phys. Rev. Lett. **68**, 534 (1992).
- G. Kido, K. Komorita, H. Katayama-Yoshida, and T. Takahashi, J. Phys. Chem. Solids **52**, 1465 (1991).

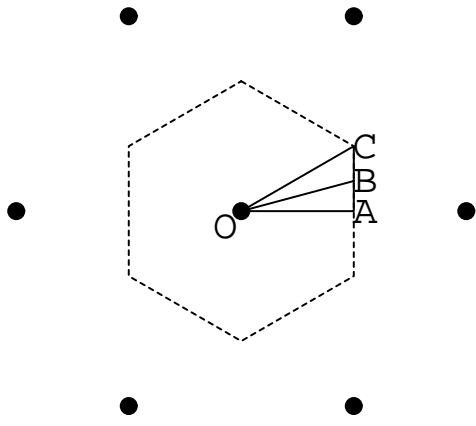


Fig. 1

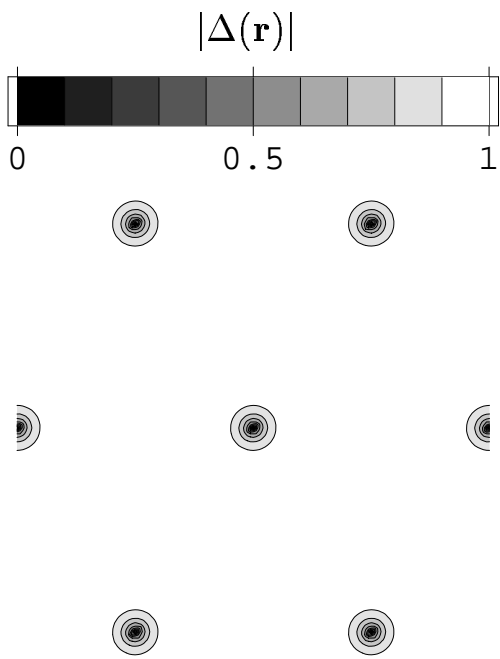


Fig. 2 (a)

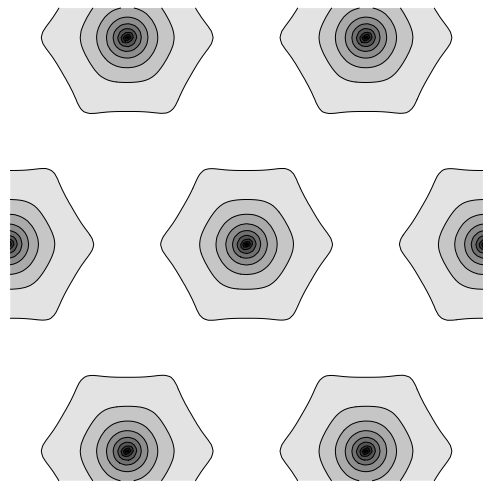


Fig. 2 (b)

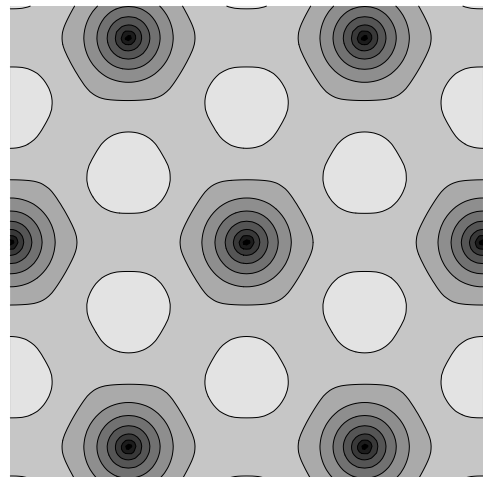


Fig. 2 (c)

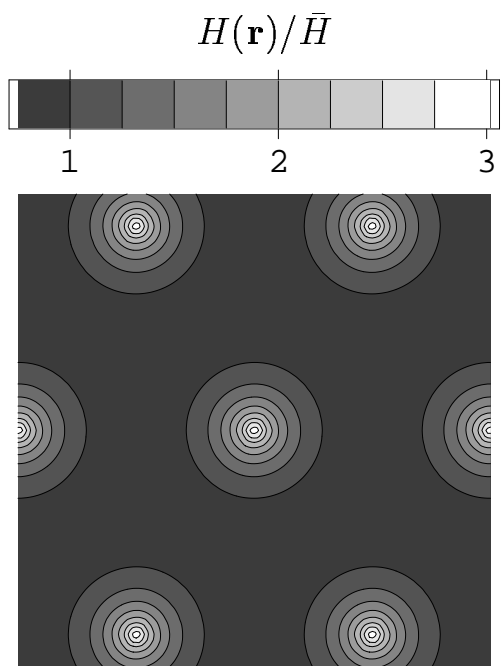


Fig. 3 (a)

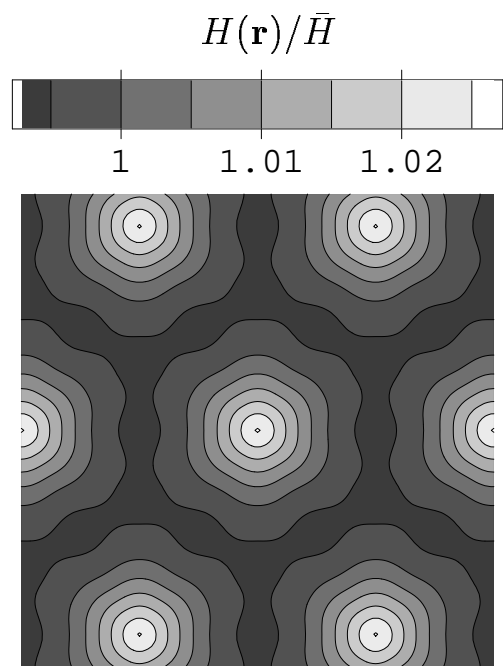


Fig. 3 (c)

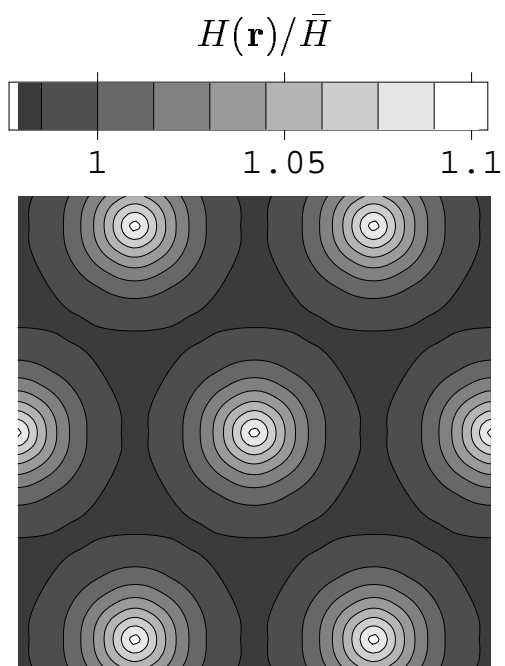


Fig. 3 (b)

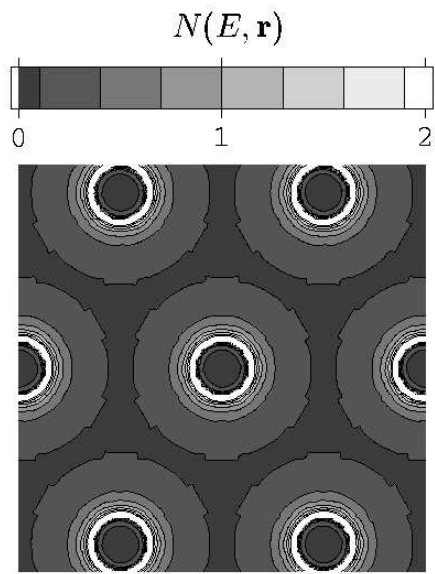


Fig. 4 (a)

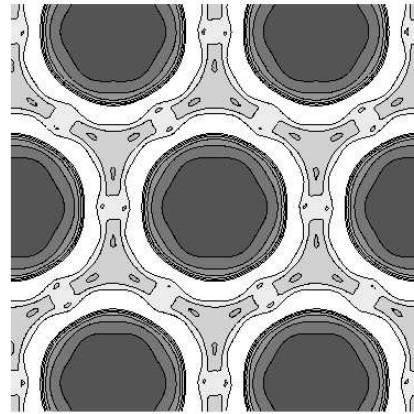


Fig. 4 (b)

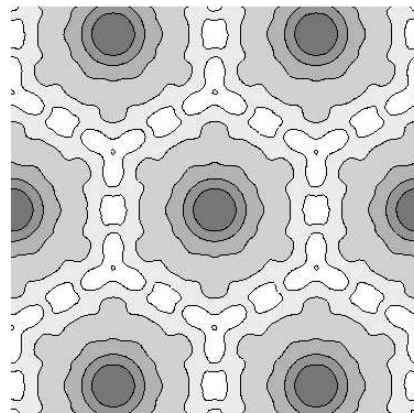


Fig. 4 (c)

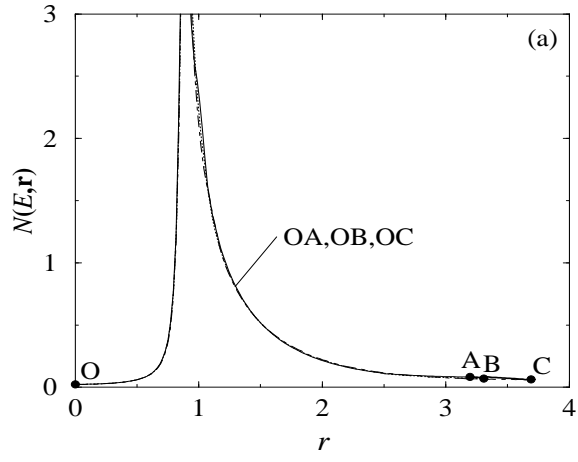


Fig. 5 (a)

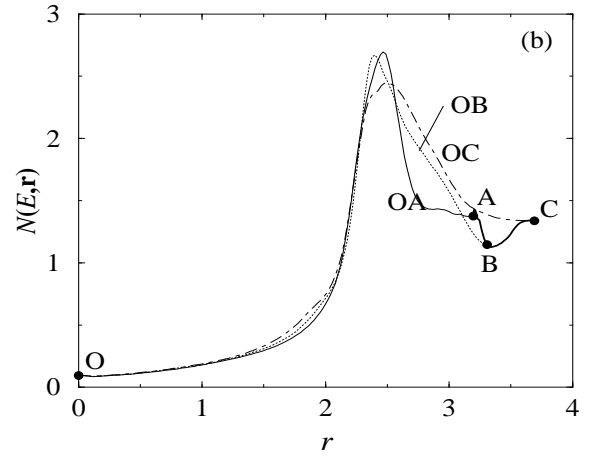


Fig. 5 (b)

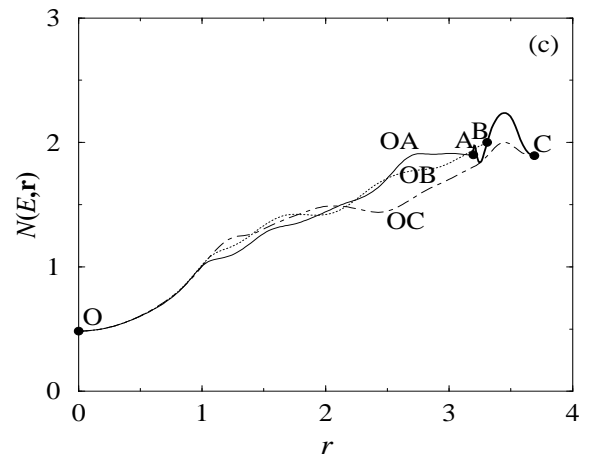


Fig. 5 (c)

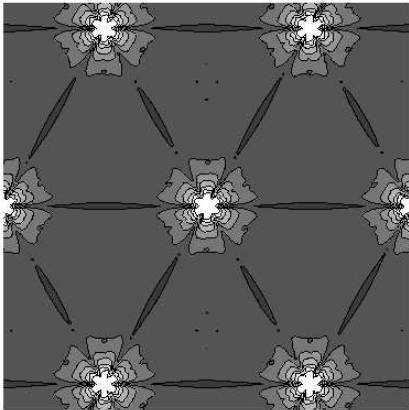


Fig. 6 (a)

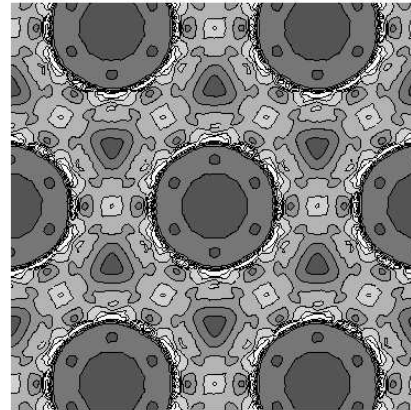


Fig. 6 (d)

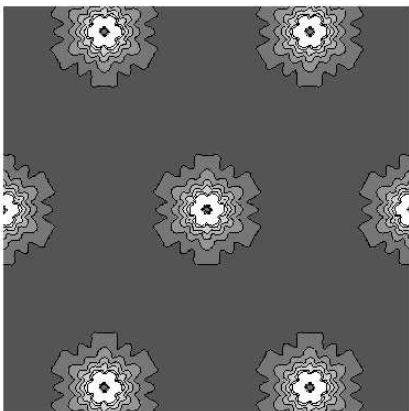


Fig. 6 (b)

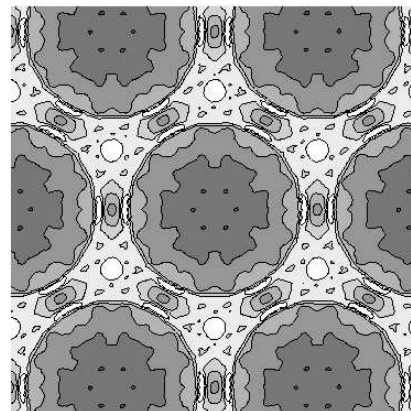


Fig. 6 (e)

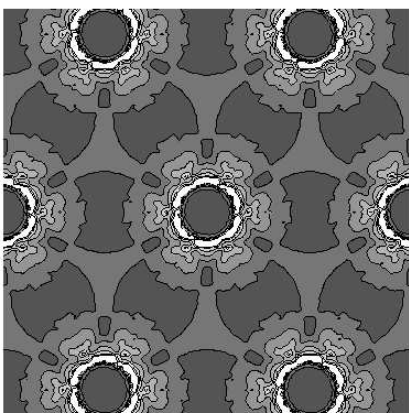


Fig. 6 (c)

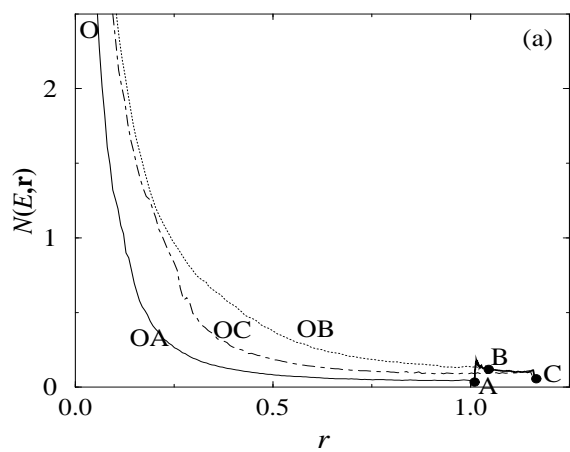


Fig. 7 (a)

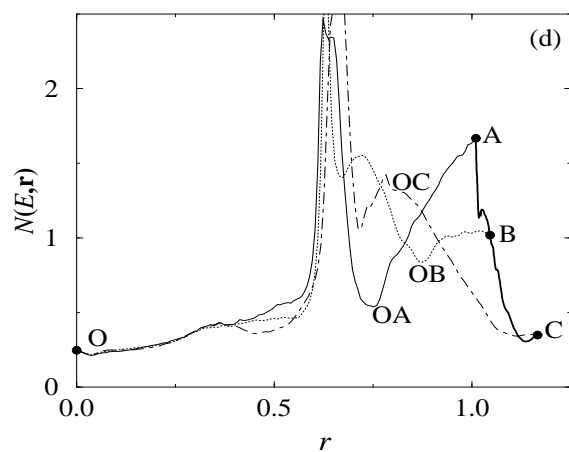


Fig. 7 (d)

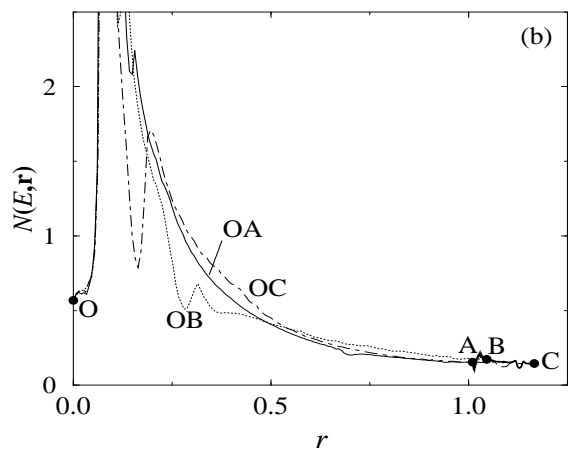


Fig. 7 (b)

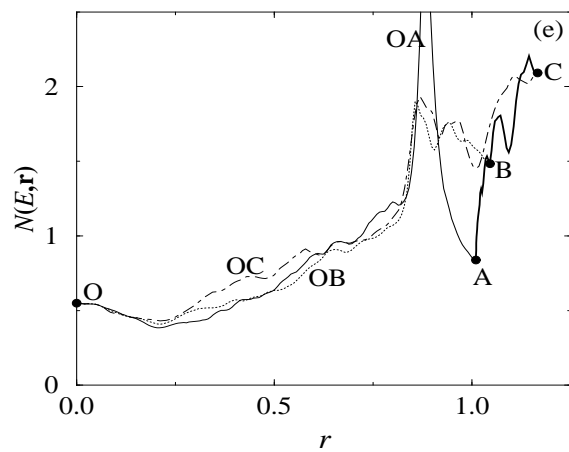


Fig. 7 (e)

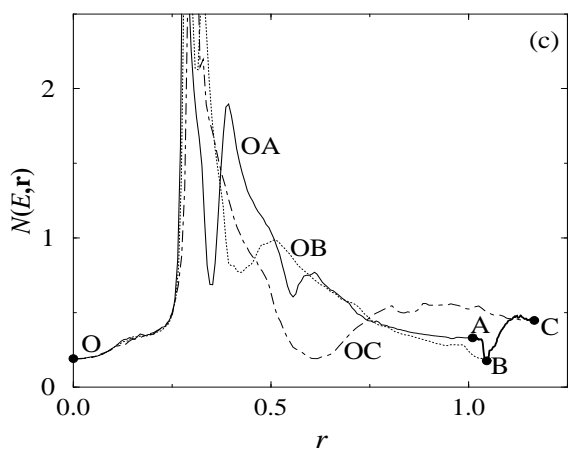


Fig. 7 (c)

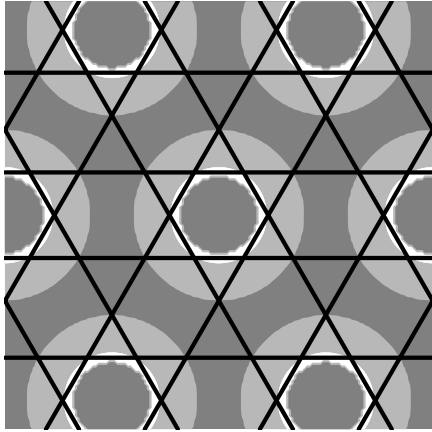


Fig.8

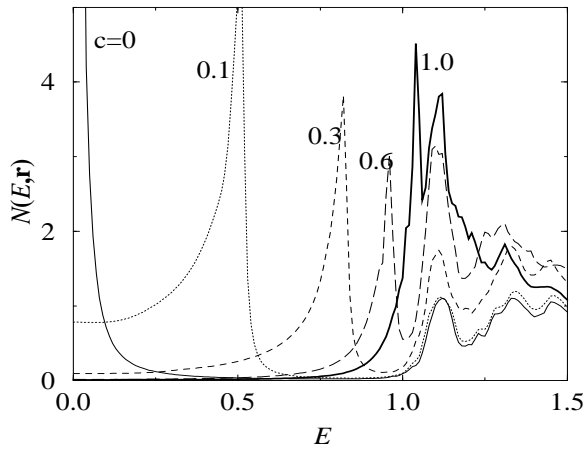


Fig. 9

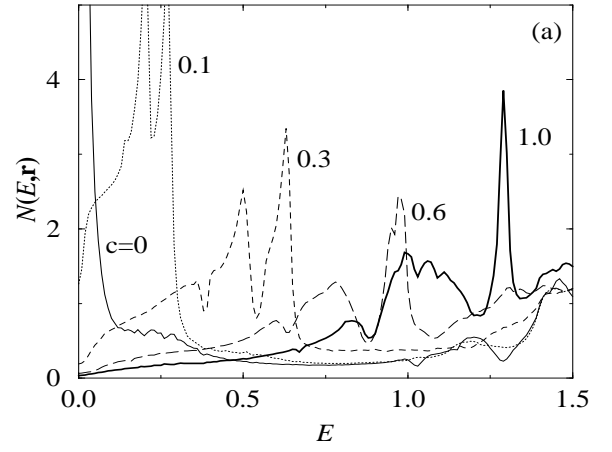


Fig. 10 (a)

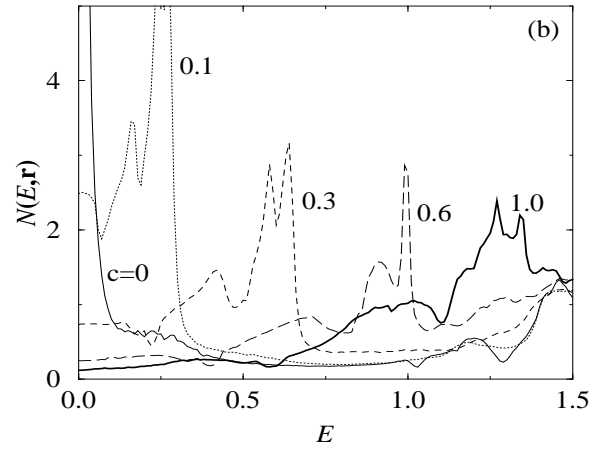


Fig. 10 (b)

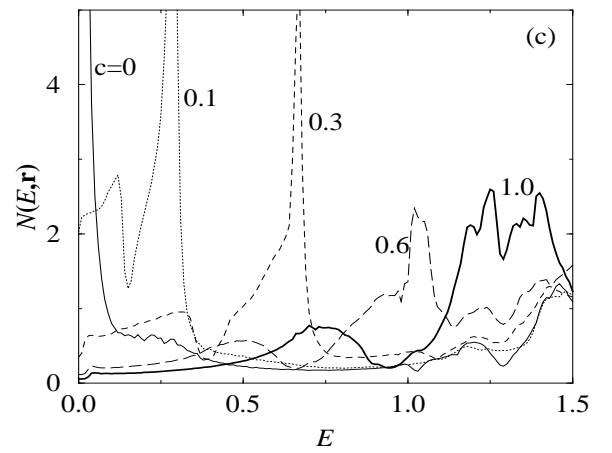


Fig. 10 (c)

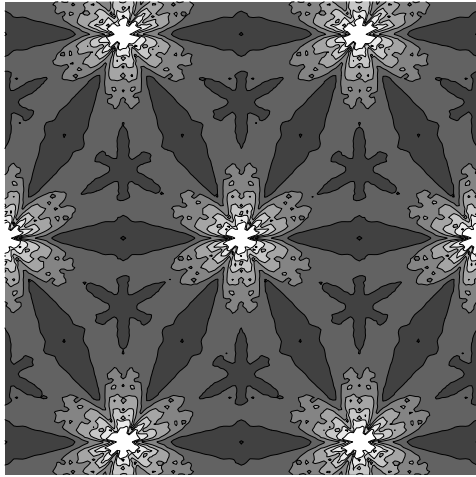


Fig. 11 (a)

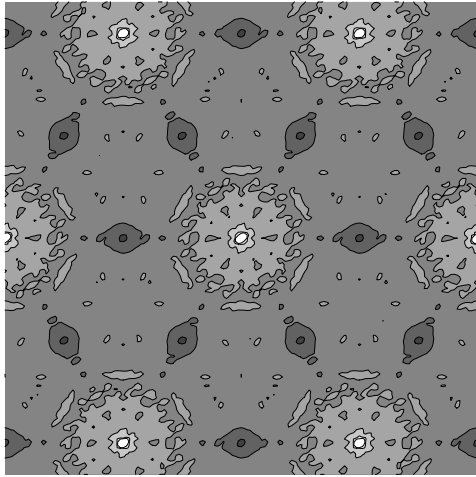


Fig. 11 (b)

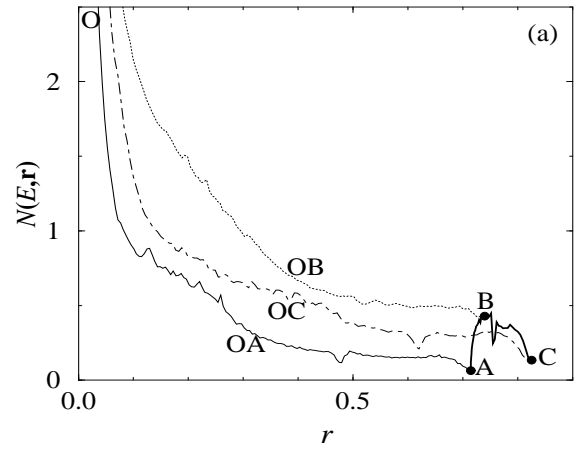


Fig. 12 (a)

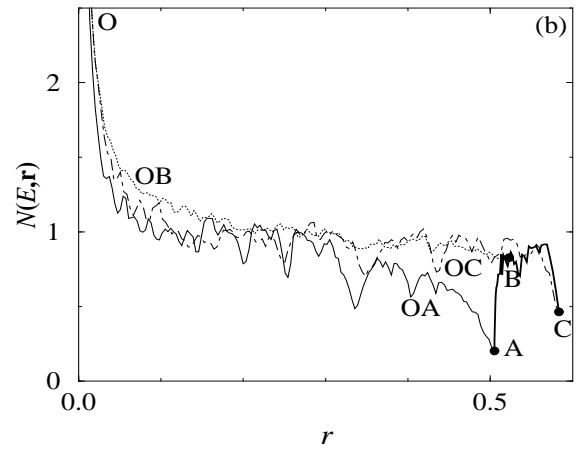


Fig. 12 (b)